Int. J. Ind. Chem. 2026; 17(1): 14-27

International Journal of Industrial Chemistry (IJIC)

https://doi.org/10.57647/ijic.2026.1701.03

Research Article

Enzymatic Urea Biosensor on Screen-Printed Carbon Electrodes Based on a Hierarchical Polypyrrole/Reduced Graphene Oxide Scaffold with Machine Learning-Assisted Analysis

Roozbeh Jamaliyan[1], Afshin Farahbakhsh[1*], Javad Mohebbi Najm Abad[2], Susan Khosroyar[1]

[1]*Department of Chemical Engineering, Qu.c., Islamic Azad University, Quchan, Iran*
[2]*Department of Computer Engineering, Qu.c., Islamic Azad University, Quchan, Iran*

[*] **Corresponding authors:** afshin.farahbakhsh@iau.ac.ir

Article History:

Received:
07 January 2026

Revised:
18 February 2026

Accepted:
15 March 2026

Published in Issue:
31 March 2026

Abstract

This study presents a cost-effective enzymatic urea biosensor developed on a screen-printed carbon electrode (SPCE) using a sequential layer-by-layer modification strategy. A conductive polypyrrole (PPy) scaffold was electrochemically deposited to mitigate the restacking of reduced graphene oxide (rGO) sheets, creating a high-surface-area matrix for the covalent immobilization of urease (Urs). Evaluated in phosphate-buffered saline (PBS), the biosensor exhibited a linear response from PBS blank (0 mM) to 30 mM urea, with a calculated limit of quantification (LOQ) of 12.17 µM, a limit of detection (LOD) of 3.65 µM, and an area-normalized sensitivity of 3.68 $\mu A \cdot mM^{-1} \cdot cm^{-2}$. The device demonstrated high precision with relative standard deviations (RSDs) below 3%, robust storage stability (93% retention after 4 weeks), and good selectivity against physiological interferents. Beyond experimental testing, an explainable machine learning (ML) workflow was used as a supportive post hoc analysis to analyze the influence of fabrication variables and to benchmark urea concentration prediction against conventional electrochemical calibration. Overall, this work presents an engineering-optimized PPy/rGO/Urs modification strategy compatible with disposable SPCE fabrication for urea sensing in PBS and provides a transparent, ML-assisted data-analysis framework for sensor optimization and interpretation under controlled bench-validation conditions.

Keywords: Machine learning; Polypyrrole; Reduced graphene oxide; Screen-printed carbon electrode; Urea biosensor; Urease

Cite this article: Jamaliyan R, Farahbakhsh A, Mohebbi Najm Abad J, Khosroyar S. Enzymatic Urea Biosensor on Screen-Printed Carbon Electrodes Based on a Hierarchical Polypyrrole/Reduced Graphene Oxide Scaffold with Machine Learning-Assisted Analysis. Int. J. Ind. Chem. 2026; 17(1): 14-27. https://doi.org/10.57647/ijic.2026.1701.03

1. Introduction

Urea is a critical biomarker for diagnosing chronic kidney disease (CKD) and monitoring metabolic health [1], with physiological concentrations ranging from ~2.5–7.5 mM in blood serum to ~20–25 mM in sweat [2,3]. Deviations from these ranges motivate the development of rapid and accessible analytical tools, including those intended for clinical and point-of-care (PoC) applications, which often involve the complex handling of biological fluids [4]. While traditional methods (e.g., spectrometry, chromatography) are accurate, their complexity and cost limit their utility in resource-limited environments [5].

In contrast, electrochemical biosensors offer a viable alternative, providing simplicity, cost-effectiveness, and miniaturization potential [6].

These sensors typically employ urease (Urs) to catalyze urea hydrolysis, generating measurable electrochemical signals [2]. However, their performance is often limited by the poor conductivity, insufficient surface area, and suboptimal electron transfer kinetics of conventional electrode materials [7,8].

To address these limitations, the integration of nanomaterials and conductive polymers is essential [9]. The combination selected in this study prioritizes performance and manufacturability: Screen-printed carbon electrodes (SPCEs) offer cost-effectiveness and scalability [10]; polypyrrole (PPy), a conductive polymer, provides enhanced conductivity and mechanical stability [11]; and reduced graphene oxide (rGO), a nanomaterial, offers a high surface area, excellent electron transfer characteristics, and a suitable substrate for Urs immobilization [12,13].

Although PPy/rGO composites have been extensively studied in electrochemical applications [14–17], along with other nanocomposites for urea detection [13,18–21], their effective implementation on SPCE platforms remains challenging. A key issue is the tendency of rGO sheets to restack through π–π interactions, which significantly limits the accessible electrochemically active surface area (EASA), particularly given the unique topography of SPCEs [22,23].

To address this specific challenge, a sequential layer-by-layer fabrication approach was developed. A porous PPy scaffold is first electrodeposited to act as a spacer, followed by drop-casting of rGO sheets, enabling electrostatic adsorption/assembly on the PPy/SPCE surface [15,23–25].

This strategy aims to maximize rGO dispersion and enhance EASA for stable Urs immobilization. Given the extensive prior literature on PPy/rGO composites and urease-based urea sensors, the contribution is positioned not as a new urea-sensing concept, but as an engineering- and manufacturability-oriented implementation on disposable SPCEs. Specifically, we (i) design a sequential PPy spacer/rGO architecture to mitigate rGO restacking on the SPCE topography and improve fabrication reproducibility for efficient Urs immobilization, and (ii) apply an explainable machine learning (ML) workflow as a supportive post hoc analysis to evaluate the effects of key fabrication/sensing variables and to benchmark concentration prediction alongside conventional electrochemical calibration, building on recent ML-assisted sensor studies [4,21,26,27]. Here, ML is used as an auxiliary tool for validation and interpretability, not as a substitute for classical electrochemical optimization; given the limited dataset size and controlled PBS conditions, the ML results are presented as supportive evidence (e.g., variable importance and consistency checks) and are not intended to support clinical decision-making.

2. Experimental

2.1. Chemicals and Apparatus

Urease (Type IX, from jack beans, Cat. No. U4002-100KU), pyrrole monomer, reduced graphene oxide (rGO), 1-ethyl-3-(3-dimethylaminopropyl) carbodiimide (EDC), and N-hydroxysuccinimide (NHS) were purchased from Sigma-Aldrich. Sulphuric acid (H_2SO_4), urea, glucose, ascorbic acid, creatinine, uric acid, potassium chloride (KCl), and potassium ferrocyanide/ferricyanide ($K_4[Fe(CN)_6]/K_3[Fe(CN)_6]$) were obtained from Merck. Phosphate-buffered saline (PBS, 20 mM) was prepared from Na_2HPO_4, KH_2PO_4, and NaCl and used as the supporting electrolyte [28]. SPCEs (DropSens DRP-110) comprised a carbon working electrode (WE, 4.0 mm diameter), a carbon counter electrode (CE), and an on-chip silver reference electrode (RE) on a ceramic substrate. Electrochemical measurements were performed using a Metrohm Autolab PGSTAT302N potentiostat/galvanostat (NOVA 2.1.7). Scanning electron microscopy (SEM) employed a LEO 1450VP. ML analysis was conducted using Python 3.9.7 with scikit-learn 1.1.2 and SHAP 0.41.0.

2.2. Electrochemical Measurements

All electrochemical measurements were conducted at 25 ± 2 °C using independently fabricated electrodes (n = 6), unless otherwise stated. Sensor characterization was performed by cyclic voltammetry (CV) and electrochemical impedance spectroscopy (EIS) in 10 mM $[Fe(CN)_6]^{3-/4-}$ solution (0.1 M KCl). CV was conducted from –0.5 V to +0.7 V (vs. Ag RE) at 50 mV/s to assess electron-transfer kinetics through anodic and cathodic peak currents (I_{pa}, I_{pc}) and peak separation (ΔE_p). EIS was performed from 0.1 Hz to 100 kHz at open-circuit potential with 10 mV amplitude to determine charge transfer resistance (R_{ct}) [29]. For quantitative analysis, differential pulse voltammetry (DPV) was conducted in 20 mM PBS from –0.6 V to +0.4 V (scan rate: 10 mV/s, pulse amplitude: 50 mV, pulse width: 50 ms). The DPV peak current served as the analytical signal for performance evaluation [13].

2.3. Biosensor Preparation and Machine Learning–Based Analysis

2.3.1. *Biosensor Fabrication and Sensing Mechanism*

The stepwise fabrication of the PPy/rGO/Urs-modified SPCE, together with the associated ML-assisted analysis workflow, is illustrated in Fig. 1. First, bare SPCEs were cleaned, dried under nitrogen, and electrochemically activated via CV (3 cycles, −2.5 to +2.5 V vs. Ag RE, 100

10.57647/ijic.2026.1701.03

mV/s) in 0.1 M H_2SO_4 [30]. A PPy scaffold was then electropolymerized onto the WE by a single CV cycle (−0.2 to +1.0 V, 20 mV/s) in a solution containing 0.025 M pyrrole and 0.25 M H_2SO_4, followed by rinsing to remove unreacted monomer [15,29]. Subsequently, 2 µL of an rGO suspension (6 g/L, ultrasonicated for 2 h) was drop-cast onto the PPy layer and dried to form the composite film (with electrostatic adsorption/assembly) [15,31]. Finally, Urs was immobilized using EDC/NHS chemistry: rGO surface carboxyl groups were activated with EDC/NHS (2 mM EDC and 5 mM NHS in PBS pH 7.0, 10 min, 25 °C), followed by incubation with 2 µL of Urs solution (5 mg/mL in PBS pH 7.0) for 1 h at 37 °C to form covalent amide bonds. The electrode was rinsed with PBS to remove unbound enzyme, yielding the final biosensor [13,15,16,32,33]. The detection principle relies on the enzymatic hydrolysis of urea:

$$(NH_2)_2CO + H_2O \rightarrow 2NH_3 + CO_2$$

In the PBS electrolyte, the reaction products form ammonium (NH_4^+), bicarbonate (HCO_3^-), and hydroxide (OH^-) ions, causing a local pH increase at the electrode surface. The PPy/rGO composite acts as a pH-sensitive transducer; the pH shift induces deprotonation and dedoping of the PPy backbone, altering the film's conductivity and electrochemical behavior. This change is recorded as a variation in the DPV peak current, which is proportional to the urea concentration [2,13,18,19].

2.3.2. *Machine Learning Modeling Strategy*

After biosensor preparation and electrochemical characterization, ML was used as a supportive analysis based on two datasets derived from the optimized platform. Dataset 1 (biochemical optimization) contained 96 observations from 16 experimental conditions (n = 6 per condition) and used Urs concentration, immobilization time, PBS pH, and response time as inputs to model the DPV peak current (output), thereby validating the fabrication/optimization workflow. Dataset 2 (urea quantification under buffered and interference conditions) contained 132 observations from 22 experimental groups (n = 6 per group) and used the DPV peak current as input to predict urea concentration (output), spanning 12 urea concentration levels (0–30 mM) together with 10 additional selectivity/interference groups to benchmark concentration-prediction performance alongside conventional electrochemical calibration. ML is used here as a supportive, post hoc analysis for validation and interpretability, not as an “ML-enhanced sensing” claim. Because the datasets are small and obtained in controlled PBS conditions, generalizability to independent batches or real clinical matrices is not claimed. Future studies should evaluate cross-batch validation and uncertainty/noise-robustness analysis to better assess model generalizability beyond controlled PBS conditions. To address the limited sample size and mitigate the risk of overfitting, a rigorous Grouped Nested Cross-Validation (GNCV) strategy was implemented [34,35]. The outer loop employed a Leave-One-Group-Out (LOGO) split for unbiased evaluation, while the inner loop utilized a four-fold GroupKFold on the training set for hyperparameter tuning via Grid Search. The use of GroupKFold ensures that all replicates of a specific experimental condition remain together in either the training or validation set, thereby preventing information leakage between replicates. To strictly avoid data leakage, all preprocessing steps, including low-variance feature removal and standardization, were performed within the cross-validation pipeline, applied solely to the training data of each fold [36]. Candidate models included linear regressors such as partial least squares (PLS), ridge regression (RR), lasso (Lasso), and elastic net (ENet), as well as non-linear models including support-vector regression (SVR), random forest (RF), histogram gradient boosting (HistGB), extra trees (ET), XGBoost (XGB), and multilayer perceptron (MLP) [26,27,37,38]. Model performance was evaluated on the unseen test data using the coefficient of determination (R^2), mean absolute error (*MAE*), and root mean squared error (*RMSE*), calculated according to Eqs. (1)–(3) [26,27,39]:

$$R^2 = 1 - \frac{\sum_{i=1}^{n}(y_i - \hat{y}_i)^2}{\sum_{i=1}^{n}(y_i - \bar{y})^2} \quad (1)$$

$$MAE = \frac{\sum_{i=1}^{n}|y_i - \hat{y}_i|}{n} \quad (2)$$

$$RMSE = \sqrt{\frac{\sum_{i=1}^{n}(y_i - \hat{y}_i)^2}{n}} \quad (3)$$

where y_i and $\hat{y}_i$ represent the observed and predicted values, $\bar{y}$ is the mean of observed values, and n is the number of samples. For these metrics, lower *MAE*/*RMSE* and higher R^2 indicate better performance. Finally, to interpret the "black-box" nature of the top-performing non-linear models, Shapley Additive Explanations (SHAP) analysis was conducted on the biochemical dataset to quantify the specific contribution of each feature to the model output [40].

3. Results and Discussion

3.1. Optimization of Fabrication and Sensing Variables

3.1.1. *Platform Fabrication and Optimization*

Stepwise SPCE modifications resulted in a suitable platform for Urs immobilization, with optimization data summarized in Table 1.

10.57647/ijic.2026.1701.03

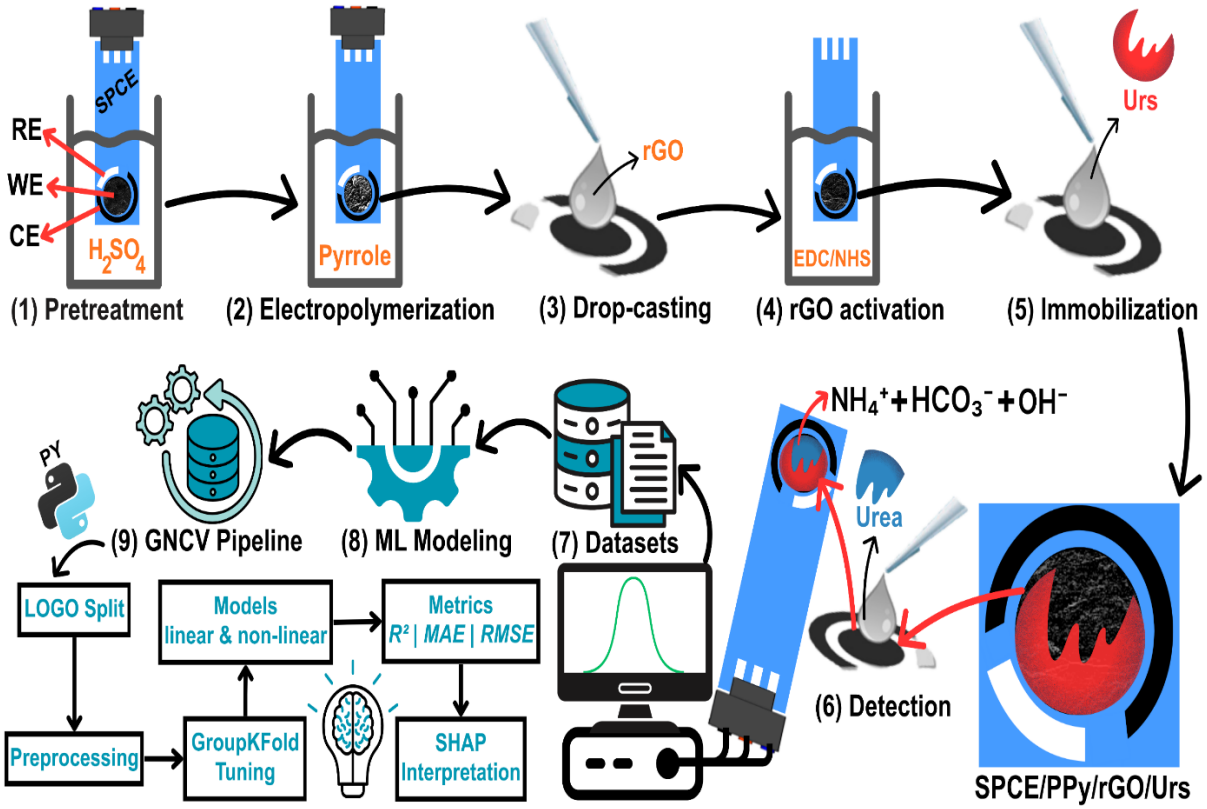

Figure 1. Workflow for preparing PPy/rGO/Urs-modified SPCEs and ML analysis of electrochemical data

First, electrochemical H_2SO_4 activation cleaned the electrode, increasing I_{pa} by ~14% and decreasing ΔE_p by ~28% compared to the inactive SPCE [41]. Next, electropolymerization with 0.025 M pyrrole further increased I_{pa} by ~89% and reduced ΔE_p by ~63% relative to the activated SPCE; notably, lower pyrrole concentrations produced incomplete films, while higher concentrations formed passivating layers [42]. Subsequently, standalone rGO deposition on the SPCE surface, even at the optimal concentration of 12 g/L, exhibited sluggish kinetics due to sheet restacking. At higher concentrations (24 g/L), this led to surface blockage and undefined peaks.

In contrast, depositing rGO onto the SPCE/PPy surface at the optimized rGO loading (6 g/L) mitigated restacking, as the PPy scaffold acted as a conductive spacer to limit sheet aggregation. This optimized configuration outperformed standalone rGO in both I_{pa} and ΔE_p [43]. Compared to PPy alone, the PPy/rGO composite delivered ~44% higher I_{pa} with only a small ΔE_p increase attributable to interfacial contact resistance, indicating that the conductivity gain outweighs the minor kinetic penalty [23,25].

Finally, a 10 min EDC/NHS activation optimally primed rGO's carboxyl groups for enzyme coupling, with shorter activations remaining incomplete and longer exposures causing NHS ester hydrolysis and signal loss [15,16,32,33]. Collectively, these optimized steps yielded a well-suited surface for Urs immobilization.

3.1.2. *Biosensing Parameter Optimization*

Following platform fabrication, the biosensor's analytical parameters were optimized using DPV at 10 mM urea (Fig. 2). A representative urea concentration of 10 mM was used for one-factor-at-a-time optimization; full calibration was then performed under the optimized conditions.

Urs at 5 mg/mL was identified as optimal; lower amounts provided insufficient catalytic sites, whereas higher amounts caused steric crowding and mass transfer limitations (Fig. 2a) [44–47]. An immobilization time of 60 min ensured complete enzyme attachment without risking denaturation associated with prolonged exposure (Fig. 2b) [13].

Similarly, a pH 7.0 buffer produced the highest signal, consistent with the optimal pH activity of free Urs (Fig. 2c) [13,46]. Finally, a 60 s response time was sufficient to reach a steady-state signal (Fig. 2d). Together, these interdependent optimizations provided a robust baseline for subsequent analytical studies.

3.2. Physicochemical and Electrochemical Characterization

3.2.1. *Surface Morphology*

SEM imaging (Fig. 3) revealed distinct morphologies at each modification stage. The bare SPCE surface exhibits a micro-rough carbon-ink topography [48].

Table 1. Optimization of electrode fabrication parameters

Optimization Step	I_{pa} (μA)	ΔE_p (mV)
Surface State		
Inactive SPCE	212.7 ± 3.5	444.8 ± 7.5
Active SPCE	241.8 ± 3.6	322.3 ± 9.0
Pyrrole (M)		
0.01	322.1 ± 2.3	365.9 ± 10.4
0.025	456.8 ± 5.5	119.2 ± 9.9
0.05	272.9 ± 2.0	318.9 ± 13.4
0.1	182.8 ± 2.1	336.5 ± 8.7
rGO (Direct) (g/L)		
3	275.7 ± 2.8	218.2 ± 11.8
6	342.6 ± 4.5	276.9 ± 11.0
12	395.4 ± 4.7	312.2 ± 11.1
24	N/A	N/A
rGO (on PPy) (g/L)		
3	560.5 ± 3.5	453.2 ± 12.3
6	655.7 ± 4.3	135.9 ± 9.0
12	386.2 ± 3.5	394.5 ± 10.4
24	269.2 ± 3.0	436.4 ± 11.8
Activation (min)		
5	556.7 ± 5.5	441.4 ± 7.6
10	531.1 ± 5.4	147.7 ± 7.6
20	303.8 ± 2.3	436.4 ± 10.4
30	N/A	N/A

CV performed in 10 mM $[Fe(CN)_6]^{3-/4-}$ (0.1 M KCl). Data: mean ± SD (n = 6). N/A: no discernible redox peaks

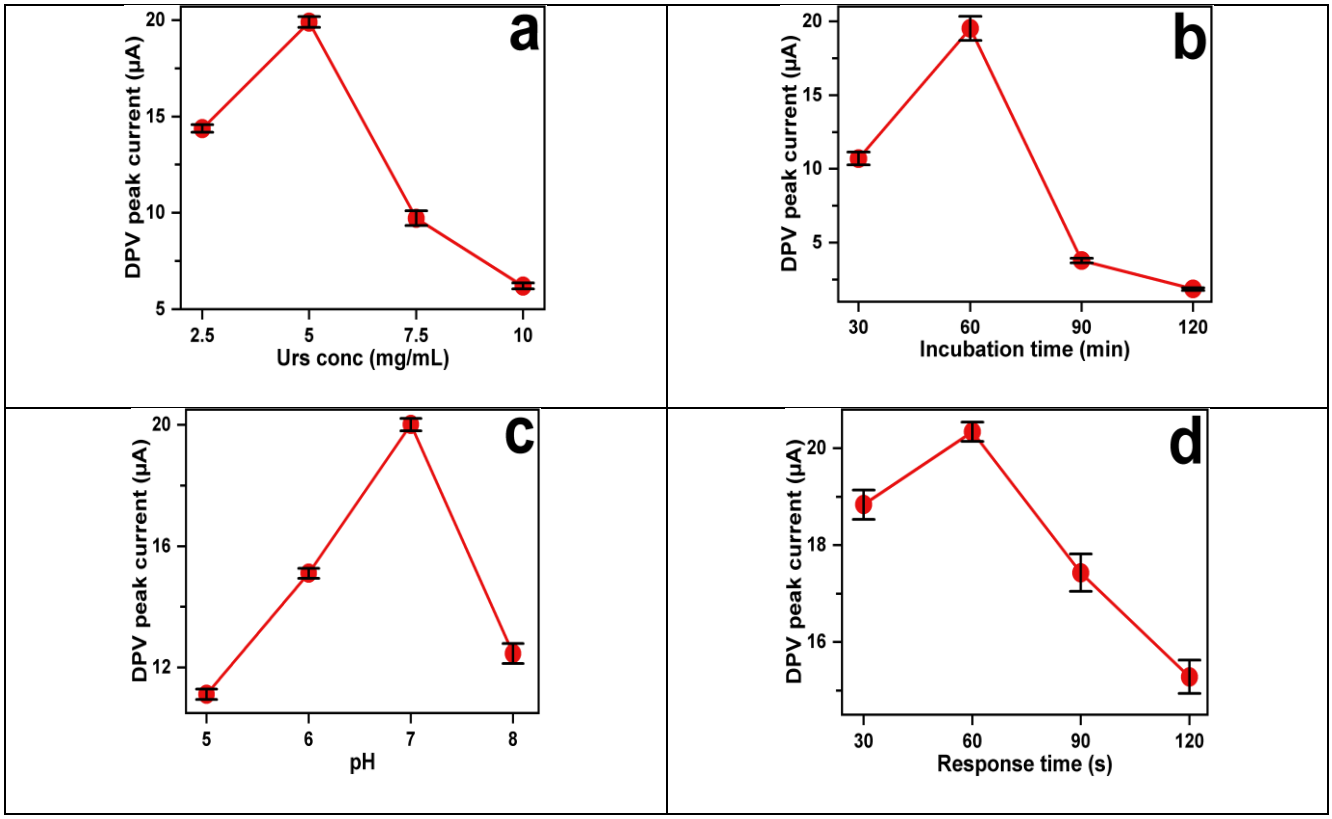

Figure 2. Optimization of biosensing parameters via DPV in 10 mM urea: (a) Urs concentration, (b) immobilization time, (c) pH, and (d) response time (mean ± SD, n = 6)

10.57647/ijic.2026.1701.03

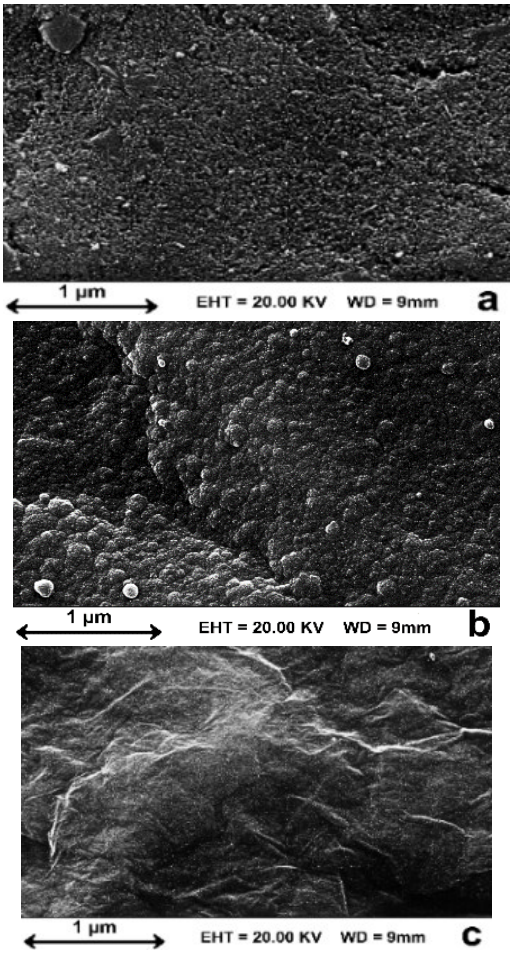

Figure 3. SEM images of (a) bare SPCE, (b) SPCE/PPy, and (c) SPCE/PPy/rGO

Electropolymerization of pyrrole forms a PPy layer with a porous, cauliflower-like network that serves as a conductive scaffold [29,49]. Subsequently, rGO deposition uniformly covers the PPy layer with wrinkled graphene sheets. Crucially, these images confirm that the PPy underlayer effectively limits rGO restacking, providing a highly accessible surface area suitable for efficient enzyme immobilization [50].

3.2.2. *Electrochemical Characterization and Validation of Enzyme Immobilization*

Electrochemical characterization was performed using CV and EIS to monitor the stepwise assembly. CV analysis (Fig. 4a) demonstrated that the optimized PPy/rGO composite increased I_{pa} by ~170% and decreased ΔE_p by ~58% compared to the activated bare SPCE, indicating significantly enhanced electron transfer kinetics. Following enzyme immobilization, I_{pa} decreased by ~34% (to ~431.4 µA) and ΔE_p increased by ~137% (to ~323 mV). This decrease in I_{pa}, together with the increase in ΔE_p, is consistent with successful enzyme immobilization, as the protein layer hinders electron transfer of the redox probe [51]. Consistently, EIS measurements of the R_{ct} (Fig. 4b) corroborated these findings. R_{ct} dropped significantly by ~76% (from ~97 Ω to ~23 Ω) after PPy modification, but subsequently rose slightly to ~30 Ω upon rGO deposition due to interflake contact resistance. Despite this minor rise, the large CV current enhancement indicates that the expanded surface area from the PPy/rGO layer outweighs the small impedance increase. Most importantly, after enzyme attachment, Rct rose sharply to ~105 Ω. This pronounced rise in R_{ct} (~250%) is consistent with formation of an insulating protein layer and substantial enzyme coverage on the rGO scaffold [52]. To validate enzymatic functionality, CV and DPV responses were measured in 10 mM urea solution.

The CV responses (Fig. 4c) showed that control electrodes (bare SPCE, SPCE/PPy, SPCE/PPy/rGO) exhibited only minimal background currents, whereas the fully modified SPCE/PPy/rGO/Urs electrode displayed a distinct anodic peak associated with urea hydrolysis. Similarly, DPV (Fig. 4d) revealed negligible background signals for the control electrodes but a pronounced catalytic peak for the enzyme-functionalized electrode.

These results demonstrate that the immobilized Urs actively catalyzes urea hydrolysis on the final electrode, generating localized pH and ionic changes that are transduced by the conductive PPy/rGO matrix into a clear electrochemical signal. This dual-technique validation confirms that the enzyme retains its biocatalytic activity and underscores the platform's effectiveness for urea detection.

10.57647/ijic.2026.1701.03

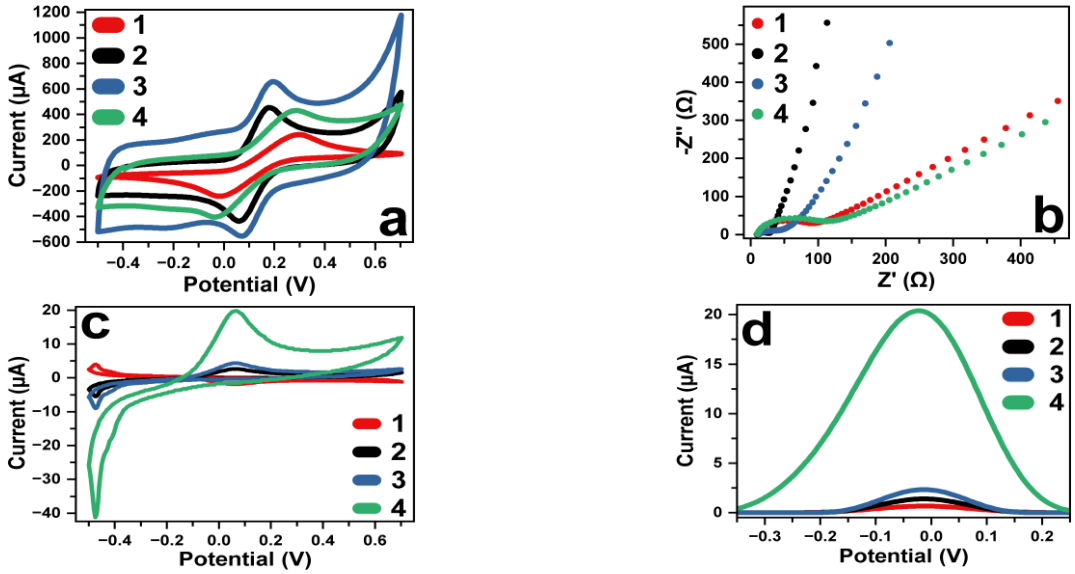

Figure 4. (a) CV and (b) EIS in 10 mM $[Fe(CN)_6]^{3-/4-}$ (0.1 M KCl); (c) CV and (d) DPV in 10 mM urea. (1) bare SPCE, (2) SPCE/PPy, (3) SPCE/PPy/rGO, (4) SPCE/PPy/rGO/Urs

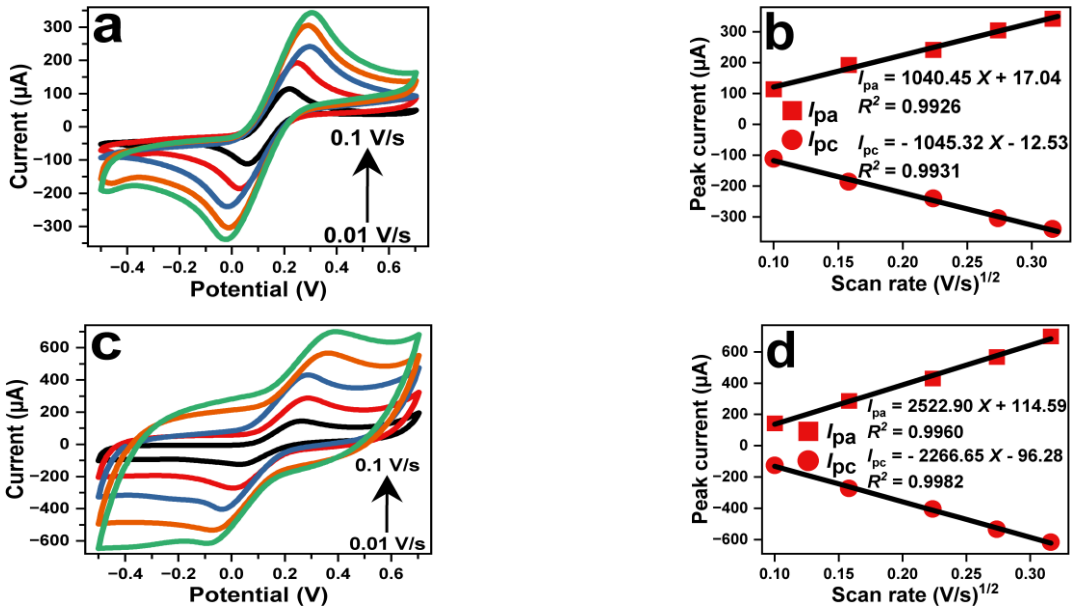

Figure 5. CVs and Randles–Sevcik plots for EASA determination in 10 mM $[Fe(CN)_6]^{3-/4-}$ (0.1 M KCl): (a, b) bare SPCE, (c, d) SPCE/PPy/rGO/Urs

3.2.3. *Electroactive Surface Area (EASA)*

To quantify the surface enhancement, scan-rate-dependent CVs were recorded for the bare SPCE and the SPCE/PPy/rGO/Urs electrode (Fig. 5). Following the methodology of Trachioti et al. [53], and since both electrodes showed $\Delta E_p > 200$ mV (indicative of irreversible redox behavior), the modified Randles–Sevcik equation for irreversible systems (Eq. 4) was employed:

$$I_p = 2.99\times10^5 AC\sqrt{\alpha D v} \quad (4)$$

Here, I_p is the peak current (A), α is the transfer coefficient, A is the electroactive surface area (cm²), D is the diffusion coefficient (7.6×10^{-6} cm²/s), C is the redox probe concentration (mol/cm³), and v is the scan rate (V/s). The transfer coefficient α, representing the apparent electron-transfer kinetics under irreversible conditions, was determined experimentally by averaging values derived from the cathodic peak potential (E_{pc}) and the half-peak potential ($E_{p/2,c}$) using Eq. 5:

$$\left|E_{Pc} - E_{p/2,c}\right| = \frac{47.7}{\alpha}\ (\text{mV, at } 25\ ^\circ\text{C}) \quad (5)$$

Based on these calculations, the average α decreased from 0.460 (bare SPCE) to 0.347 (SPCE/PPy/rGO/Urs), consistent with increased kinetic irreversibility of the redox probe after Urs immobilization. The decrease in α is therefore interpreted as an indicator of increased kinetic irreversibility caused by protein-layer-induced interfacial blocking/heterogeneity, rather than a contradiction to the enhanced net surface accessibility provided by the PPy/rGO scaffold; this interpretation is also consistent

10.57647/ijic.2026.1701.03

with the increased ΔE_p and R_{ct} observed after Urs immobilization (Fig. 4a–b).

Using the slopes of the corresponding Randles–Sevcik plots (Fig. 5) with these α values, the apparent EASA was calculated as 0.187 cm² for bare SPCE and 0.467 cm² for SPCE/PPy/rGO/Urs. Although enzyme immobilization is intrinsically passivating, the PPy/rGO hierarchical scaffold substantially increases surface roughness and forms a percolated conductive network; therefore, even after Urs deposition, a large fraction of the scaffold remains electrochemically accessible to the redox probe. Accordingly, the EASA reported for the final SPCE/PPy/rGO/Urs electrode should be interpreted as an apparent/operational electroactive area under the sensing configuration, which provides a relevant basis for areal normalization of the measured response. Furthermore, the surface roughness factor, defined as EASA divided by the geometric area of the WE (0.126 cm²), rose from 1.49 for bare SPCE to 3.72 for the final biosensor, confirming the superior functional surface area provided by the 3D scaffold.

3.3. Electroanalytical Performance

3.3.1. *Linear Range, Sensitivity, and Limit of Detection*

The quantitative performance of the biosensor was assessed using DPV in buffered urea solutions (Fig. 6). The sensor exhibited a linear response from PBS blank (0 mM) to 30 mM urea (Fig. 6a). The corresponding calibration plot (Fig. 6b) reveals an excellent linear relationship (R^2 = 0.998) between the peak current and urea concentration. From the slope of this plot, the sensitivity was determined to be 1.72 μA·mM⁻¹. Normalizing this value to the electroactive surface area (0.467 cm²) yielded an areal sensitivity of 3.68 μA·mM⁻¹·cm⁻² [26].

The limit of detection (LOD) and limit of quantification (LOQ) were calculated using standard criteria (LOD = 3σ/S and LOQ = 10σ/S), where S is the sensitivity (slope) and σ is the standard deviation of the blank signal (determined from ten independent blank measurements) [13,54,55]. Based on these parameters, the biosensor achieved an LOD of 3.65 μM and an LOQ of 12.17 μM.

3.3.2. *Selectivity and Interference Study*

Biosensor selectivity was evaluated against common interferents at physiologically relevant concentrations, including NaCl (150 mM), KCl (10 mM), glucose (5 mM), ascorbic acid (1 mM), creatinine (1 mM), and uric acid (1 mM). The relative response (*RR*) for each interferent was calculated using Eq. 6:

$$RR\,(\%) = \frac{I_i - I_b}{I_u - I_b} \times 100\,\% \qquad (6)$$

where I_i is the mean peak current for the interfering substance, I_u is the mean peak current for 1 mM urea, and I_b is the mean background current of the PBS blank. As shown in Fig. 7a, with 1 mM urea as the reference (100%), all individual interferents produced an *RR* below 10% [13]; KCl showed the largest individual effect (~9.5%), while the others remained between ~2–5%. In a mixed-interferent PBS condition containing 1 mM urea and all interferents, the signal increased by ~14.6% relative to urea alone.

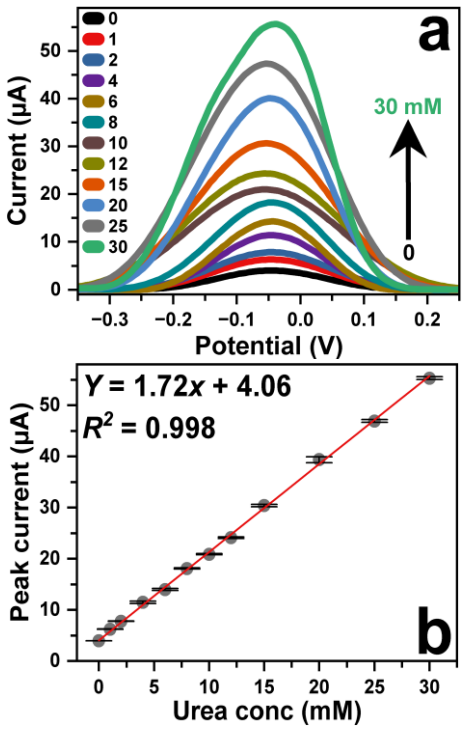

Figure 6. (a) DPV responses for 0–30 mM urea; (b) Calibration: peak current vs. urea conc. Data: mean ± SD (n = 6).

10.57647/ijic.2026.1701.03

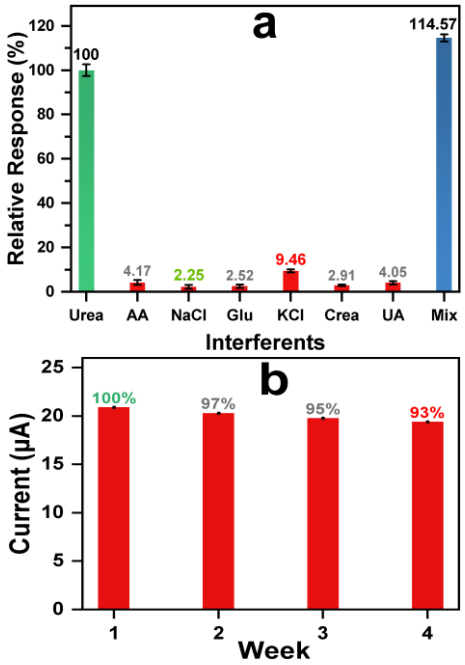

Figure 7. Evaluation of biosensor reliability: (a) selectivity against common interfering species (mean ± SD, $n = 6$); and (b) storage stability in 10 mM urea over 4 weeks

Table 2. Statistical analysis of sensor reliability

Parameter	Repeatability	Reproducibility
Test 1 (μA)	20.91	20.65
Test 2 (μA)	20.52	21.42
Test 3 (μA)	20.25	20.36
Test 4 (μA)	19.87	20.95
Test 5 (μA)	19.73	21.17
Mean ± SD	20.26 ± 0.48	20.91 ± 0.41
RSD (%)	2.37	2.00

Data represent the DPV response to 10 mM urea

Although this combined interference slightly exceeds the 10% threshold for single species, it is notably lower than the theoretical sum of individual interferences (~25.2%), suggesting that competitive surface interactions may limit the cumulative effect [46,47]. All selectivity and interference experiments were conducted in PBS; therefore, matrix effects relevant to urine/serum (e.g., fouling, buffering, and non-specific interactions) were not evaluated and remain a limitation requiring future validation in spiked synthetic matrices and real samples.

3.3.3. *Reproducibility, Repeatability, and Stability*

The reliability of the biosensor was evaluated via repeatability, reproducibility, and storage stability (Table 2, Fig. 7b).

Repeatability (intra-assay precision) measured at 10 mM urea yielded a relative standard deviation (RSD) of 2.37% over five consecutive measurements. Reproducibility (inter-assay precision) across five independently fabricated electrodes resulted in an RSD of 2.0%, indicating consistent fabrication.

Long-term storage stability was assessed by storing sensors in PBS (pH 7.0) at 4 °C. As depicted in Fig. 7b, the biosensor retained 93% of its initial response after 4 weeks. This modest signal loss is consistent with gradual enzyme deactivation, confirming the effective stabilization provided by the biocompatible PPy/rGO matrix.

3.4. Machine Learning Analysis of Biosensor Performance

Following experimental data collection, a benchmarking study was conducted to evaluate ML models using two datasets focused on (i) biochemical optimization (dataset 1) and (ii) urea concentration prediction under buffered and interference conditions (dataset 2). The comparative performance of the evaluated models is summarized in Table 3. For dataset 1, linear regressors consistently showed limited predictive capability ($R^2 \approx 0.41$), indicating that the fabrication/sensing variables introduce non-linear interactions not captured by simple linear relationships. In contrast, ensemble methods—particularly XGBoost—achieved markedly higher predictive accuracy ($R^2 > 0.99$), consistent with non-linear relationships within the present dataset [56]. For dataset 2, where the sensor's intrinsic linearity primarily reflects the urea-only PBS calibration subset (0–30 mM; Section

10.57647/ijic.2026.1701.03

3.3.1) and the remaining groups probe PBS-based interference/selectivity (Section 3.3.2), linear regressors already delivered near-perfect performance ($R^2 > 0.993$; Table 3), reflecting the sensor's highly linear and low-noise response. Tree-based models (RF/ET) achieved lower *RMSE* than linear regressors within dataset 2 (Table 3) [57]. However, because conventional linear calibration already performs strongly and the evaluation is limited to a small PBS-based dataset without external validation, these ML results are presented as supportive benchmarking rather than evidence for generalizable performance gains or clinical deployment/decision-making. The agreement between predicted and experimental values for the best-performing models for each dataset is shown in Fig. 8a–b.

Table 3. Performance evaluation of regression models for biochemical optimization and urea sensing.

Dataset	Model	R^2	MAE	RMSE
Dataset 1	PLS	0.41211	3.751	4.422
	RR	0.40288	3.850	4.457
	Lasso	0.40823	3.811	4.437
	ENet	0.40363	3.856	4.454
	SVR (RBF)	0.99017	0.468	0.571
	RF	0.98721	0.526	0.652
	ET	0.99020	0.474	0.571
	XGBoost	0.99052	0.464	0.561
	HistGB	-0.01965	4.922	5.824
	MLP	0.99031	0.472	0.567
Dataset 2	PLS	0.993412	0.48381	0.75371
	RR	0.993411	0.48383	0.75373
	Lasso	0.993410	0.48387	0.75375
	ENet	0.993410	0.48387	0.75375
	SVR (RBF)	0.987513	0.67749	1.03761
	RF	0.999602	0.06291	0.18502
	ET	0.999621	0.05603	0.18069
	XGBoost	0.982750	0.41845	1.21956
	HistGB	0.948051	0.78665	2.11643
	MLP	0.992085	0.49274	0.82606

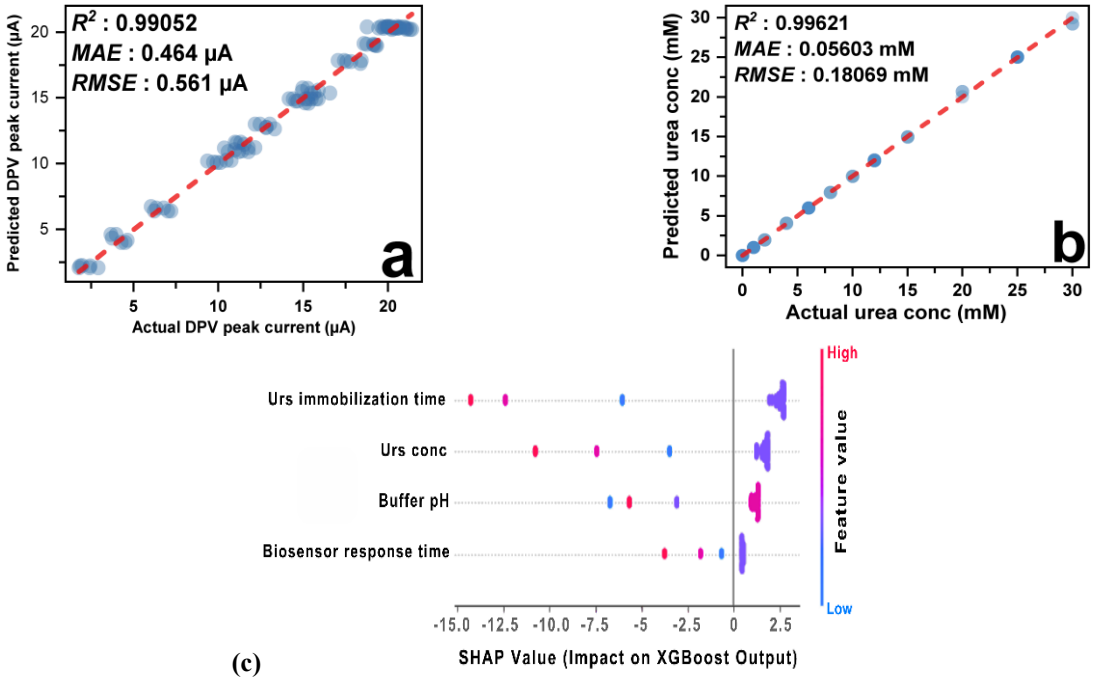

Figure 8. Evaluation of ML models: (a) Predicted vs. experimental DPV currents using XGBoost; (b) Predicted vs. actual urea concentrations using ET; and (c) SHAP summary plot for feature importance

10.57647/ijic.2026.1701.03

Table 4. Analytical performance benchmarking of the proposed biosensor against recently reported enzymatic urea sensors

Sensing Platform	Matrix	ML Integration	Linear range (mM)	Sensitivity	LOD (μM)	Reference
SPCE/AgrGO	PBS	No	0 – 10	47.598 ($\mu A \cdot \mu M^{-1} \cdot cm^{-2}$)	0.16	[13]
Pt/PPy-NiO	PBS	No	0.7 – 26.7	0.153 ($mA \cdot mM^{-1} \cdot cm^{-2}$)	1.6	[18]
Pt/PPy	PBS	No	1.67–8.32	0.0035 ($mA \cdot mM^{-1}$)	2570	[19]
Pt/MPPy	PBS	No	0.5–10.82	0.0432 ($mA \cdot mM^{-1}$)	208	[19]
GR/TrGO	PBS	No	0.2 – 12	2.3 ($\mu A \cdot mM^{-1} \cdot cm^{-2}$)	20	[20]
SPCE/PPy/rGO	PBS	Yes	0 – 30	3.68 ($\mu A \cdot mM^{-1} \cdot cm^{-2}$)	3.65	This Work

To further bridge the gap between "black-box" ML predictions and electrochemical reality, SHAP analysis was utilized for the non-linear biochemical optimization dataset (Fig. 8c). The feature importance ranking identifies immobilization time and enzyme concentration as the dominant contributors to the modeled response within dataset 1.

Importantly, this ranking is consistent with the experimentally observed optimization trends (Fig. 2), supporting internal consistency between the ML analysis and the electrochemical results rather than establishing a new mechanistic conclusion.

SHAP dependence plots further suggest stronger effects of Urs concentration and immobilization time within the tested range, while PBS pH and response time show comparatively smaller contributions under the present conditions.

3.5. Comparative Evaluation of the Biosensor

Table 4 benchmarks the proposed biosensor against recently reported enzymatic urea sensors, including graphene-derived and PPy-modified electrode platforms. Direct sensitivity comparisons across studies should be interpreted cautiously due to differences in transduction mode, electrode geometry, normalization, and testing conditions; therefore, Table 4 is intended primarily for contextual benchmarking rather than definitive performance ranking. The comparison highlights trade-offs among reported sensitivity, operational range, and material/fabrication complexity. Notably, noble-metal-doped platforms (e.g., silver–reduced graphene oxide, AgrGO) are often reported to achieve higher sensitivities and lower detection limits in PBS, consistent with the electrocatalytic contribution of silver nanoparticles; however, cross-study differences in normalization, electrode geometry, and testing conditions limit direct ranking. In contrast, the proposed metal-free SPCE/PPy/rGO architecture prioritizes cost-efficiency, fabrication reproducibility, and compatibility with disposable SPCE formats while maintaining analytically useful performance in PBS. Moreover, whereas the AgrGO-based sensor reports a linear range limited to 0–10 mM, the developed device exhibits a broader linear response from PBS blank (0 mM) to 30 mM urea. In comparison to platinum-based composites, the performance landscape highlights a conflict between cost and catalytic efficiency. While complex architectures like platinum/polypyrrole–nickel oxide (Pt/PPy-NiO) demonstrate low detection limits—benefiting from the synergistic electrocatalytic contribution of nickel oxide—these designs inherently rely on cost-intensive platinum.

Conversely, other platinum variants such as standard Pt/PPy or macroporous Pt/MPPy report higher detection limits and/or narrower linear ranges than those obtained here under controlled PBS conditions, suggesting that the added analytical benefit may not always justify the higher material cost for disposable formats.

Furthermore, Table 4 provides contextual benchmarking against representative carbon-based alternatives (e.g., GR/TrGO), highlighting trade-offs among reported sensitivity, linear range, and cost for disposable formats. Finally, as highlighted in Table 4, we implemented an explainable ML-based analysis to support optimization and calibration; such analyses have not been reported in the studies summarized in Table 4.

4. Conclusions

This study demonstrates an engineering-optimized and cost-effective urea-sensing configuration on disposable SPCEs using a sequential PPy/rGO scaffold for covalent Urs immobilization. The sequential modification strategy was designed to mitigate graphene-sheet restacking and yielded a high-surface-area conductive scaffold that supported effective Urs immobilization.

Analytical evaluation in PBS demonstrated that the optimized device offers a linear response from PBS blank (0 mM) to 30 mM urea, with a calculated LOQ of 12.17 μM. The sensor delivered a sensitivity of 3.68 $\mu A \cdot mM^{-1} \cdot cm^{-2}$, an LOD of 3.65 μM, together with high precision (repeatability and reproducibility RSDs of 2.37% and 2.00%, respectively) and storage stability (93% retention after 4 weeks). Furthermore, an explainable ML workflow was applied as a supportive post hoc analysis to analyze how fabrication variables influence the

electrochemical response and to benchmark concentration prediction alongside conventional electrochemical calibration. Within the present dataset, non-linear models (XGBoost and ET) provided strong fits between fabrication variables and signal output ($R^2 > 0.99$), while SHAP analysis offered interpretable feature attributions, highlighting immobilization time and Urs concentration as the most influential features in this dataset. Given the limited dataset size and the controlled PBS conditions, these ML results are presented as supportive validation and interpretation and do not imply clinical decision-making capability without external validation.

Comparative benchmarking indicates an engineering trade-off: although the metal-free PPy/rGO architecture shows lower analytical sensitivity than some noble-metal-based systems, it offers a practical balance of operational range, cost-effectiveness, and fabrication reproducibility, while remaining compatible with disposable SPCE fabrication. Accordingly, the present work should be interpreted as a PBS-based methodological and engineering validation of the proposed biosensor architecture. A key limitation of this study is that analytical validation was performed only in PBS; therefore, matrix effects in complex biological media (e.g., urine and serum) were not evaluated. Further validation in spiked synthetic and real biological matrices, together with device-level integration, is required before assessing practical feasibility or any future PoC relevance.

Acknowledge

This work is part of the Ph.D. thesis of Roozbeh Jamaliyan at Islamic Azad University, Quchan Branch. The authors thank the staff of the Chemistry Laboratory of Islamic Azad University, Quchan Branch, for technical support and access to instrumentation and facilities.

Authors Contribution

Conceptualization, A.F. and R.J.; Methodology, R.J.; Software and ML modeling, J.M.N.A. and R.J.; Validation and Formal analysis, R.J. and J.M.N.A.; Investigation, Resources, Data curation, R.J.; Visualization, R.J.; Writing – original draft, R.J.; Writing – review and editing, R.J., S.Kh., and A.F.; Supervision and Project administration, A.F. and S.Kh. All authors have read and approved the final version of the manuscript.

Availability of data and materials

The data that support the findings of this study are available from the corresponding author, upon reasonable request.

Conflict of interests

The author states that there is no conflict of interest.

References

[1] Tan HT, Liu Q, Teo TL. Advancing accuracy in chronic kidney disease diagnosis and management: reference materials and reference measurement procedures for clinical markers. Ann Lab Med. 2025;45(4):367-380. https://doi.org/10.3343/alm.2024.0583

[2] Mashhadban-K F, Gorgani L, Najafpour-Darzi G. Enzymatic electrochemical biosensors for urea detection: a review. Sens Actuators A Phys. 2024;374:115499. https://doi.org/10.1016/j.sna.2024.115499

[3] Laochai T, Moonla C, Moon JM, Sakdaphetsiri K, Yin L, Mendes LF, et al. Touch-based potentiometric sensors for simultaneous detection of urea and ammonium from fingertip sweat. Sens Actuators B Chem. https://doi.org/10.1016/j.snb.2024.135898

[4] Thiyyadi D, Vandana R, Shankar B, Vijayan L. Electrochemical biosensors for urea detection: recent trends and future perspectives. Microchem J. https://doi.org/ 10.1016/j.microc.2025.115805

[5] Magar HS, Hassan RYA, Abbas MN. Non-enzymatic disposable electrochemical sensors based on CuO/Co3O4@MWCNTs nanocomposite modified screen-printed electrode for the direct determination of urea. Sci Rep. 2023; 13:2034. https://doi.org/10.1038/s41598-023-28930-4

[6] Kim J, Jeong J, Ko SH. Electrochemical biosensors for point-of-care testing. Bio-Des Manuf. 2024; 7:548-565. https://doi.org/10.1007/s42242-024-00301-6

[7] Zeng R, Qiu M, Wan Q, Huang Z, Liu X, Tang D, et al. Smartphone-based electrochemical immunoassay for point-of-care detection of SARS-CoV-2 nucleocapsid protein. Anal Chem. 2022; 94:15155-15161. https://doi.org/ 10.1021/acs.analchem.2c03606

[8] Liu Y, Zhao X, Liao M, Ke G, Zhang XB. Point-of-care biosensors and devices for diagnostics of chronic kidney disease. Sens Diagn. 2024; 3:1789-1806. https://doi.org/ 10.1039/d4sd00241e

[9] Ahmadian I, Kargar Razi M, Sadeghi B, Nakhaei M. Synthesis of photocatalytic material based on polyaniline supported PVC/NiAl2O3/AlF3 nanocomposite. Int J Ind Chem. 2024;15(2):15241 https://doi.org/ 10.57647/j.ijic.2024.1502.16

[10] Paimard G, Ghasali E, Baeza M. Screen-printed electrodes: fabrication, modification, and biosensing applications. Chemosensors. 2023;11(2):113. https://doi.org/ 10.3390/chemosensors11020113

[11] Zhang X, Tan X, Wang P, Qin J. Application of polypyrrole-based electrochemical biosensor for the early diagnosis of colorectal cancer. Nanomaterials https://doi.org/ 10.3390/nano13040674

[12] Wang Y, Shi N, Kang X, Pan Q, Tian M, Wang Y, et al. Sensitive competitive electrochemical immunosensor for Hg(II) based on molybdenum disulfide/reduced graphene oxide/gold nanocomposites. Sensors. 2025;25(3):623. https://doi.org/ 10.3390/s25030623

[13] Ashakirin SN, Haniff MASM, Zaid MHM, Razipwee MFM, Mahmoudi E. Urease immobilized electrodeposited silver reduce graphene oxide modified screen-printed carbon electrode for highly urea detection. Measurement. 2022;196:111058. https://doi.org/10.1016/j.measurement.2022.111058

[14] Bao J, Hou C, Zhao Y, Geng X, Samalo M, Yang H, et al. An enzyme-free sensitive electrochemical microRNA-16 biosensor by applying a multiple signal amplification strategy based on

Au/PPy-rGO nanocomposite as a substrate. Talanta. 2019; 196:329-336. https://doi.org/ 10.1016/j.talanta.2018.12.082

[15] Rezapoor-Fashtali Z, Ganjali MR, Faridbod F. A novel electrochemical aptasensor based on a new platform of samarium molybdate flower-like nanoparticles@poly(pyrrole) for non-invasive determination of saliva cortisol. Biosensors. https://doi.org/ 10.3390/bios12090720

[16] Chang HM, Zhang Y, Hashimoto C, Vazquez CI, Fang Y, Kumar P, et al. Sensitive detection of SARS-CoV-2 spike antibodies by a paper-based polypyrrole/reduced graphene oxide sensor. Biotechnol Bioprocess Eng. 2025; 30:80-87. https://doi.org/10.1007/s12257-024-00150-1

[17] Haroun AA, Kamel S, Elnahrawy AM, Hammad AA, Hamadneh I, Al-Dujaili AH. Polyacetal/graphene/polypyrrole and cobalt nanoparticles electroconducting composites. Int J Ind Chem. https://doi.org/10.1007/s40090-020-00218-w

[18] Hosseinian M, Darzi GN, Rahimpour A. A novel bioelectrochemical sensor based on immobilized urease on the surface of nickel oxide nanoparticle and polypyrrole composite modified Pt electrode. Electroanalysis. 2019; 31:2530-2537. https://doi.org/ 10.1002/elan.201800862

[19] Hosseinian M, Najafpour G, Rahimpour A. Amperometric urea biosensor based on immobilized urease on polypyrrole and macroporous polypyrrole modified Pt electrode. Turk J Chem. 2019; 43:1063-1074. https://doi.org/ 10.3906/kim-1901-13

[20] Razumiene J, Gureviciene V, Sakinyte I, Rimsevicius L, Laurinavicius V. The synergy of thermally reduced graphene oxide in amperometric urea biosensor: application for medical technologies. Sensors. https://doi.org/ 10.3390/s20164496

[21] Mohebbi Najm Abad J, Farahbakhsh A, Mir M, Alizadeh R, Hekmatmanesh A. Urea-self powered biosensors: a predictive evolutionary model for human energy harvesting. Sensors. 2023;23(19):8180. https://doi.org/ 10.3390/s23198180

[22] Abdillah OB, Rus YB, Ulfa M, Dedi, Iskandar F. Recent progress on reduced graphene oxide and polypyrrole composites for high performance supercapacitors: a review. J Energy Storage. 2023; 74:109300. https://doi.org/10.1016/j.est.2023.109300

[23] James N, Krishna A, Joseph AS, B SP. Enhancing the electrochemical performance of rGO-based ternary composite for next generation supercapacitors. RSC Adv. https://doi.org/ 10.1039/d5ra05408g

[24] Li J, Östling M. Prevention of graphene restacking for performance boost of supercapacitors-a review. Crystals. https://doi.org/ 10.3390/cryst3010163

[25] Cai C, Fu J, Zhang C, Wang C, Sun R, Guo S, et al. Highly flexible reduced graphene oxide@polypyrrole-polyethylene glycol foam for supercapacitors. RSC Adv. https://doi.org/ 10.1039/d0ra05199c

[26] Zalke JB, Bhaiyya ML, Jain PA, Sakharkar DN, Kalambe J, Narkhede NP, et al. A machine learning assisted non-enzymatic electrochemical biosensor to detect urea based on multi-walled carbon nanotube functionalized with copper oxide micro-flowers. https://doi.org/ 10.3390/bios14100504

[27] Farahbakhsh A, Abad JMN, Hekmatmanesh A, Handroos H. Evaluating the performance of ethanol electrochemical nanobiosensor through machine for predictive analysis of electric current in self-powered biosensors. Battery Energy. 2024;4:e20240044. https://doi.org/ 10.1002/bte2.20240044

[28] Kim K, Lee J, Moon BM, Seo YB, Park CH, Park M, et al. Fabrication of a urea biosensor for real-time dynamic fluid measurement. Sensors. 2018;18(8):2607. https://doi.org/ 10.3390/s18082607

[29] Shafaat A, Faridbod F. Overoxidized polypyrrole/gold nanoparticles composite modified screen-printed voltammetric sensor for quantitative analysis of methadone in biological fluids. Anal Bioanal Electrochem. 2022;14(4):319-330. Publisher

[30] Barthasarathy PR, Ahmed NA, Salim WWAW. Reduced graphene oxide on screen-printed carbon electrodes as biosensor for Escherichia coli O157:H7 detection. Proceedings. 2020;60(1):13. https://doi.org/ 10.3390/IECB2020-07056

[31] Ismail NAB, Ahmed NA, Abd-Wahab F, Ramli NI, Salim WWAW. Detection of nonspecific binding of E. coli O157:H7 on reduced graphene oxide screen-printed carbon electrodes using electrochemical methods. Preprints [Preprint]. 2018:1-18. https://doi.org/ 10.20944/preprints201810.0631.v1

[32] Stanković V, Đurđić S, Ognjanović M, Antić B, Kalcher K, Mutić J, et al. Anti-human albumin monoclonal antibody immobilized on EDC-NHS functionalized carboxylic graphene/AuNPs composite as promising electrochemical HSA immunosensor. J Electroanal Chem. 2020; 860:113928. https://doi.org/ 10.1016/j.jelechem.2020.113928

[33] Venegas CJ, Rodríguez L, Sierra-Rosales P. Selective label-free electrochemical aptasensor based on carbon nanotubes for carbendazim detection. Chemosensors. 2023;11(2):117 https://doi.org/ 10.3390/chemosensors11020117

[34] Parvandeh S, Yeh HW, Paulus MP, McKinney BA. Consensus features nested cross-validation. Bioinformatics. 2020;36(10):3093-3098. https://doi.org/ 10.1093/bioinformatics/btaa046

[35] Allgaier J, Pryss R. Cross-validation visualized: a narrative guide to advanced methods. Mach Learn Knowl Extr. 2024;6(2):1378-1388. https://doi.org/ 10.3390/make6020065

[36] Moscovich A, Rosset S. On the cross-validation bias due to unsupervised preprocessing. J R Stat Soc Ser B Stat Methodol. 2022;84(4):1474-1498. https://doi.org/ 10.1111/rssb.12537

[37] Hussain I, Ching KB, Uttraphan C, Tay KG, Noor A. Evaluating machine learning algorithms for energy consumption prediction in electric vehicles: a comparative study. Sci Rep. 2025;15:16124. https://doi.org/ 10.1038/s41598-025-94946-7

[38] Sekeroglu B, Ever YK, Dimililer K, Al-Turjman F. Comparative evaluation and comprehensive analysis of machine learning models for regression problems. Data Intell. 2022;4(3):637-669 https://doi.org/ 10.1162/dint_a_00155

[39] Chellamani N, Albelwi SA, Shanmuganathan M, Amirthalingam P, Alharbi EM, Alatawi HQS, et al. A deep sparse capsule network for non-invasive blood glucose level estimation using a PPG sensor. Sensors. 2025;25(6):1868 https://doi.org/10.3390/s25061868

[40] Lundberg SM, Lee SI. A unified approach to interpreting model predictions. Adv Neural Inf Process Syst. 2017;30:4765-4774 https://doi.org/ 10.48550/arXiv.1705.07874

[41] Wan H, Sun Q, Li H, Sun F, Hu N, Wang P. Screen-printed gold electrode with gold nanoparticles modification for simultaneous electrochemical determination of lead and copper. Sens Actuators B Chem. 2015;209:336-342. https://doi.org/ 10.1016/j.snb.2014.11.127

[42] Lu L, Seenivasan R, Wang YC, Yu JH, Gunasekaran S. An electrochemical immunosensor for rapid and sensitive detection of mycotoxins fumonisin B1 and deoxynivalenol. Electrochim Acta. 2016;213:89-97 https://doi.org/ 10.1016/j.electacta.2016.07.088

[43] Sahoo PK, Kumar N, Jena A, Lee CP, Lee SY, Park SJ. Recent progress in graphene and its derived hybrid materials for high-performance supercapacitor electrode applications. RSC Adv. 2024; 14:1284. https://doi.org/ 10.1039/d3ra06904d

[44] Atailia S, Baraket A, Rabai S, Benounis M, Jaffrezic N, Araar H, et al. Electrochemical urea biosensor based on *Proteus mirabilis* urease immobilized over polyaniline PANi-glassy carbon electrode. Electroanalysis. https://doi.org/ 10.1002/elan.202200502

[45] Bié J, Sepodes B, Fernandes PCB, Ribeiro MHL. Enzyme immobilization and co-immobilization: main framework, advances and some applications. Processes. https://doi.org/ 10.3390/pr10030494

[46] Huang YM, Lin JC, Settu K. Detection of urea in human blood using graphene-based amperometric biosensor. J Electrochem Soc. 2024;171:077522. https://doi.org/ 10.1149/1945-7111/077522

[47] Bucur B, Purcarea C, Andreescu S, Vasilescu A. Addressing the selectivity of enzyme biosensors: solutions and perspectives. Sensors. 2021;21(9):3038. https://doi.org/ 10.3390/s21093038

[48] Jiménez-Fiérrez F, González-Sánchez MI, Jiménez-Pérez R, Iniesta J, Valero E. Glucose biosensor based on disposable activated carbon electrodes modified with platinum nanoparticles electrodeposited on poly(Azure A). Sensors. 2020;20(16):4489 https://doi.org/ 10.3390/s20164489

[49] Zidarič T, Majer D, Maver T, Finšgar M, Maver U. The development of an electropolymerized, molecularly imprinted polymer (MIP) sensor for insulin determination using single-drop analysis. Analyst. 2023;148:1102-1112 https://doi.org/ 10.1039/d2an02025d

[50] Zhao X, Zuo J, Qiu S, Hu W, Wang Y, Zhang J. Reduced graphene oxide-modified screen-printed carbon (rGO-SPCE)-based disposable electrochemical sensor for sensitive and selective determination of ethyl carbamate. Food Anal Methods. 2017; 10:3279-3286. https://doi.org/ 10.1007/s12161-017-0886-2

[51] Verma S, Choudhary J, Singh KP, Chandra P, Singh SP. Uricase grafted nanoconducting matrix based electrochemical biosensor for ultrafast uric acid detection in human serum samples. Int J Biol Macromol. 2019;129:778-786 https://doi.org/ 10.1016/j.ijbiomac.2019.02.121

[52] Wcisło A, Małuch I, Niedziałkowski P, Ossowski T, Prahl A. Label-free electrochemical test of protease interaction with a peptide substrate modified gold electrode. Chemosensors. 2021;9(8):199. https://doi.org/10.3390/chemosensors9080199

[53] Trachioti MG, Lazanas AC, Prodromidis MI. Shedding light on the calculation of electrode electroactive area and heterogeneous electron transfer rate constants at graphite screen-printed electrodes. Microchim Acta. 2023;190:251 https://doi.org/ 10.1007/s00604-023-05832-w

[54] Bounegru AV, Apetrei C. Voltammetric sensors based on nanomaterials for detection of caffeic acid in food supplements. Chemosensors. 2020;8(2):41. https://doi.org/ 10.3390/chemosensors8020041

[55] Gunache RO, Apetrei C. Determination of diosmin in pharmaceutical products with chemically modified voltammetric sensors. Int J Mol Sci. 2021;22(14):7315. https://doi.org/ 10.3390/ijms22147315

[56] Liu B, Liu P, Wang Y, Li Z, Lv H, Lu W, et al. Explainable machine learning for multiscale thermal conductivity modeling in polymer nanocomposites with uncertainty quantification. Compos Struct. 2025; 370:119292. https://doi.org/ 10.1016/j.compstruct.2024.119292

[57] Wang K, Gao M, Mukundan R, Gelda R, Frei A. Application of tree-based machine learning models to predict phosphorus levels in a water supply stream. J Hydroinform. 2025;27(8):1292-1308. https://doi.org/10.2166/hydro.2025.025